
Higher Order Correlations within Cortical Layers Dominate Functional Connectivity in Microcolumns

Urs Köster

Redwood Center for Theoretical Neuroscience
UC Berkeley

Jascha Sohl-Dickstein

Department of Applied Physics
Stanford University

Charles M Gray

Cellular Biology and Neuroscience
Montana State University Bozeman

Bruno A Olshausen

Redwood Center for Theoretical Neuroscience
UC Berkeley

Abstract

We report on simultaneous recordings from cells in all layers of visual cortex and models developed to capture the higher order structure of population spiking activity. Specifically, we use Ising, Restricted Boltzmann Machine (RBM) and semi-Restricted Boltzmann Machine (sRBM) models to reveal laminar patterns of activity. While the Ising model describes only pairwise couplings, the RBM and sRBM capture higher-order dependencies using hidden units. Applied to 32-channel polytrode data recorded from cat visual cortex, the higher-order models discover functional connectivity preferentially linking groups of cells within a cortical layer. Both RBM and sRBM models outperform Ising models in log-likelihood. Additionally, we train all three models on spatiotemporal sequences of states, exposing temporal structure and allowing us to predict spiking from network history. This demonstrates the importance of modeling higher order interactions across space and time when characterizing activity in cortical networks.

1 Introduction

Electrophysiology is rapidly moving towards high density recording techniques capable of capturing the simultaneous activity of large populations of neurons. This raises the challenge of understanding how networks encode and process information in ways that go beyond feedforward receptive field models for individual neurons. Modeling the distribution of states in a network provides a way to discover communication patterns and functional connectivity between cells.

The Ising model, originally developed in the 1920s to describe magnetic interactions [1], has been used to describe electrophysiological data, particularly in the retina [2], and more recently for cortical recordings [3]. This model treats spikes from a population of neurons binned in time as binary vectors and captures dependencies between cells with the maximum entropy distribution for pairwise correlation. However, this only provides a good approximation for small groups of cells in the retina [4].

In this work, we apply maximum entropy models to data from the visual cortex. Cortical networks have proven to be more challenging to model than the retina: even the existence of significant pairwise correlations between cortical cells is controversial [5, 6] and higher order correlations play an important role [7, 8, 9]. One of the challenges with current recording technologies is that we cannot simultaneously record from more than a tiny fraction of the cells that make up a cortical circuit. Sparse sampling together with the complexity of the circuit mean that the majority of a cell's input will be from cells that are not part of the recording. In adult cat visual cortex, direct synaptic connections have been reported to occur between 11% - 30% of nearby pairs of excitatory

neurons in layer IV [10], while a larger fraction of cell pairs show “polysynaptic” couplings [11], defined by a broad peak in the cross-correlation between two cells. This type of coupling can be due to common inputs (either from a different cortical area or in the form of lateral connections) or a series of monosynaptic connections. A combination of these is believed to give rise to most of the statistical interactions between the recorded cells. The Ising model, which assumes only pairwise couplings, is well suited to model direct synaptic coupling, but cannot deal with interactions that include many cells simultaneously. Therefore, we propose a new approach, that addresses both incomplete sampling and tentative inputs from larger scale cell assemblies. We extend the Ising model with a layer of hidden units or latent variables. The resulting model is a semi-Restricted Boltzmann Machine (sRBM), which combines pairwise connections between visible units with an additional set of connections to hidden units.

Estimating the parameters of Ising models and Boltzmann machines is hard because probabilities are only defined up to a normalization constant. For both Ising models and Boltzmann machines with hidden units, this normalization constant is computationally intractable, requiring a sum over the exponential number of states of the system. This makes exact maximum likelihood estimation impossible for all but the smallest systems and has previously necessitated approximate and/or computationally expensive estimation methods. In this work, we use Minimum Probability Flow (MPF [12, 13], in the context of neural decoding see [14]) to estimate parameters efficiently without computing the intractable partition function. This allows us to estimate Ising models on higher-dimensional data than is otherwise feasible, and to estimate the sRBM in a straightforward way. Similar to parameter estimation, model evaluation is also hampered by the fact that the learned models are not normalized. To compute probabilities and compare the likelihood of different models, annealed importance sampling [15] was used to estimate the partition function.

Combining these two methods for model estimation and evaluation, we show that the sRBM can capture the distribution of states in a cortical network of tens of cells recorded from cat visual cortex significantly better than a pairwise model. The higher order structure discovered by the model is spatially organized and specific to cortical layers, indicating that networks within individual layers of a microcolumn are the dominant source of correlations. Applied to spatiotemporal patterns of activity, the model captures temporal structure in addition to dependencies across different cells, allowing us to predict spiking activity based on the history of the network.

2 Methods

2.1 Recording and experimental procedures

Data were recorded from anesthetized cat visual cortex in response to a custom set of full field natural movie stimuli. Movies of 8 to 30 minutes duration were captured at 300 frames per second and 512×384 pixel resolution with a Casio F1 camera. Care was taken to avoid scene changes and camera motion, so the spatiotemporal statistics of the movie correspond to those of natural scene motion. Movies were converted to grayscale and down-sampled to 150 Hz for presentation. The high frame rate was chosen to prevent cells phase locking to the frame rate, and scene changes were minimized to avoid evoked potentials due to sudden luminance changes. Fig 1c) shows an example frame crop from one of the natural scene movies.

Recordings were made with single shank 32 channel polytrodes (Fig. 1a) with a channel spacing of $50\mu\text{m}$, spanning all the layers of visual cortex. Individual datasets had on the order of 20 to 40 simultaneously recorded neurons. The data was spike sorted offline using k-means clustering (KlustaKwik, [16]) with a manual cleanup step (MClust, [17]). Unless noted otherwise, spikes were binned at 20ms where bins with a single spike (2.4% of bins) and multiple spikes (0.9% of bins) were both treated as spiking and the rest as non-spiking. The bin size was chosen to span the width of the central peak in cross-correlograms between pairs of cells such as shown in 1e), where the dashed vertical lines at $\pm 20\text{ms}$ envelope the central peak. An example of binned data for 23 isolated single units is shown in 1b) with black marks indicating spiking.

To register individual recording channels with cortical layers, recording locations were reconstructed from Nissl-stained histological sections, and current source density analysis in response to flashed full-field stimuli was used to infer the location of cortical layer IV on the polytrode [18]. In 1b) we use horizontal lines to indicate the upper and lower boundaries of layer IV.

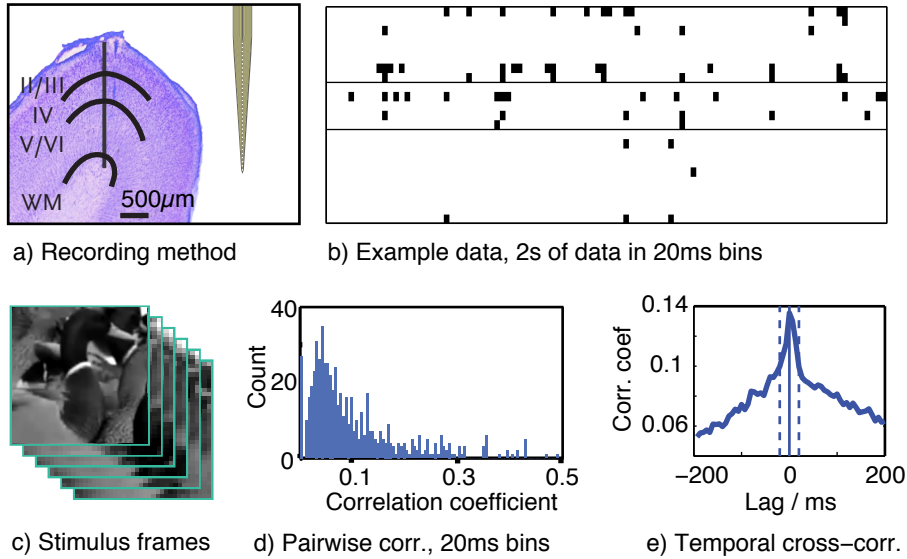


Figure 1: **(a)** Recordings were made from columns of cat visual cortex. The 32 channel probe is shown to scale. **(b)** Example data from 23 cells, binned in 20ms windows, 2s of data. Columns of this matrix are the input to our algorithm. For the spatiotemporal version of the model, we concatenate several adjacent columns. **(c)** Example of one of the natural movie stimuli presented, showing a group of ducks. **(d)** Histogram of instantaneous correlations between pairs of cells. **(e)** Cross-correlation as a function of time lag between a pair of cells binned at 6.7ms shows a peak in the correlation about 20ms wide (dashed lines). This determines the window size for binning the data.

The surgical methods are described in detail elsewhere [19]. The protocol used in the experiments was approved by the Institutional Animal Care and Use Committee at Montana State University and conformed to the guidelines recommended in Preparation and Maintenance of Higher Mammals During Neuroscience Experiments, National Institutes of Health Publication 913207 (National Institutes of Health, Bethesda, MD 1991).

The models were estimated on a data set of 180,000 data vectors corresponding to 60 minutes of recording time. The data were split into two subsets of 90,000 data points: a training set for parameter estimation and a test set to compute cross-validated likelihoods.

We also analyzed spatiotemporal patterns of data, which were created by concatenating consecutive state vectors. For the spatiotemporal experiments a bin width of 6.7 ms, corresponding to the frame rate of the stimulus, was used. This bin size is a compromise capturing more detailed structure in the data without leading to an undue increase in dimensionality and complexity. Up to 10 time bins were concatenated in order to discover spatiotemporal patterns and predict spiking given the history over the prior 67ms. These models were trained on 100,000 samples and likelihoods were computed on a set of equal size.

2.2 Model and Estimation

The sRBM consists of a set of binary visible units $\mathbf{x} \in \{0, 1\}^N$ corresponding to observed neurons in the data and a set of hidden units $\mathbf{h} \in \{0, 1\}^M$ that capture higher order dependencies. Weights between visible units, corresponding to an Ising model or fully visible Boltzmann machine, capture pairwise correlations in the data. Weights between visible and hidden units, corresponding to an RBM, learn to describe higher order structure.

The Ising model with visible-visible coupling weights $\mathbf{J} \in \mathcal{R}^{N \times N}$ and biases $\mathbf{b} \in \mathcal{R}^N$ has an energy function

$$E_I(\mathbf{x}) = -\mathbf{x}^T \mathbf{J} \mathbf{x} - \mathbf{b}^T \mathbf{x}, \quad (1)$$

with associated probability distribution $p_I(\mathbf{x}) = \frac{1}{Z_I} \exp[-E_I(\mathbf{x})]$, where the normalization constant, or partition function, $Z_I = \sum_{\{\mathbf{x}'\}} \exp[-E_I(\mathbf{x}')]$ consists of a sum over all 2^N system states.

The RBM with visible-hidden coupling weights $\mathbf{W} \in \mathcal{R}^{N \times M}$ and hidden and visible biases $\mathbf{b}_v \in \mathcal{R}^N$ and $\mathbf{b}_h \in \mathcal{R}^M$ has an energy function

$$E_R(\mathbf{x}, \mathbf{h}) = -\mathbf{x}^T \mathbf{W} \mathbf{h} - \mathbf{b}_v^T \mathbf{x} - \mathbf{b}_h^T \mathbf{h}, \quad (2)$$

with associated probability distribution $p_R(\mathbf{x}, \mathbf{h}) = \frac{1}{Z_R} \exp[-E_R(\mathbf{x}, \mathbf{h})]$. Since there are no connections between hidden units (hence ‘‘restricted’’ Boltzmann machine), the latent variables \mathbf{h} can be analytically marginalized out of the distribution (see Appendix A) to obtain

$$p(\mathbf{x}) = \int d\mathbf{h} p(\mathbf{x}, \mathbf{h}) = \frac{1}{Z_R} \exp[-E_R(\mathbf{x})], \quad (3)$$

where the energy for the marginalized distribution over \mathbf{x} (sometimes referred to as the free energy in machine learning literature) is

$$E_R(\mathbf{x}) = -\sum_i \log(1 + e^{\mathbf{w}_i^T \mathbf{x} + b_{h,i}}) - \mathbf{b}_v^T \mathbf{x}, \quad (4)$$

where \mathbf{w}_i are rows of the matrix \mathbf{W} . The energy function for an sRBM combines the Ising model and RBM energy terms,

$$E_S(\mathbf{x}, \mathbf{h}) = -\mathbf{x}^T \mathbf{J} \mathbf{x} - \mathbf{x}^T \mathbf{W} \mathbf{h} - \mathbf{b}_v^T \mathbf{x} - \mathbf{b}_h^T \mathbf{h}. \quad (5)$$

As with the RBM, it is straightforward to marginalize over the hidden units for an sRBM,

$$p_S(\mathbf{x}) = \frac{1}{Z_S} \exp[-E_S(\mathbf{x})], \quad (6)$$

$$E_S(\mathbf{x}) = -\mathbf{x}^T \mathbf{J} \mathbf{x} - \sum_i \log(1 + e^{\mathbf{w}_i^T \mathbf{x} + b_{h,i}}) - \mathbf{b}_v^T \mathbf{x}. \quad (7)$$

A hierarchical Markov Random Field based on the sRBM has previously been applied as a model for natural image patches [20], with the parameters estimated using contrastive divergence (CD, [21]).

Instead of CD, which is based on sampling, we train the models using Minimum Probability Flow (MPF, [12]), a recently developed estimation method for energy based models. MPF works by minimizing the KL divergence between the data distribution and the distribution which results from moving slightly away from the data distribution towards the model distribution. This KL divergence will be uniquely zero in the case where the model distribution is identical to the data distribution. While CD is a stochastic heuristic for parameter update, MPF provides a deterministic and easy to evaluate objective function. Second order gradient methods can therefore be used to speed up optimization considerably. The MPF objective function

$$K = \sum_{\mathbf{x} \in \mathcal{D}} \sum_{\mathbf{x}' \notin \mathcal{D}} g(\mathbf{x}, \mathbf{x}') \exp\left(\frac{1}{2} [E(\mathbf{x}) - E(\mathbf{x}')]\right) \quad (8)$$

measures the flow of probability out of data states \mathbf{x} into neighboring non-data states \mathbf{x}' , where the connectivity function $g(\mathbf{x}, \mathbf{x}') \in \{0, 1\}$ identifies neighboring states, and \mathcal{D} is the list of data states. We consider the case where the connectivity function $g(\mathbf{x}, \mathbf{x}')$ is set to connect all states which differ by a single bit flip

$$g(\mathbf{x}, \mathbf{x}') = \begin{cases} 1 & H(\mathbf{x}, \mathbf{x}') = 1 \\ 0 & \text{otherwise} \end{cases}, \quad (9)$$

where $H(\mathbf{x}, \mathbf{x}')$ is the Hamming distance between \mathbf{x} and \mathbf{x}' . See Appendix B¹ for a derivation of the MPF objective function and gradients for the sRBM, RBM, and Ising models. In all experiments, minimization of K was performed with the MinFunc implementation of L-BFGS [22].

To prevent overfitting all models were estimated with an L_1 sparseness penalty on the coupling parameters. This was done by adding a term of the form $\lambda \sum_{i,j} |J_{ij}| + \lambda \sum_{j,k} |W_{jk}|$ to the objective

¹Code is available for download at <http://github.com/Sohl-Dickstein>

function, summing over the absolute values of the elements of both the visible and hidden weight matrices. The optimal sparseness λ was chosen by cross-validating the log-likelihood on a holdout set.

Since MPF learning does not give an estimate of the partition function, we use annealed importance sampling (AIS, [15]) to compute normalized probabilities. AIS is a sequential Monte Carlo method that works by gradually morphing a distribution with a known normalization constant (in our case a uniform distribution over \mathbf{x}) into the distribution of interest. See Appendix C for more detail. AIS applied to RBM models is described in [23], which also highlights the shortcomings of previously used deterministic approximations.

Normalizing the distribution via AIS allows us to compute the log likelihood of the model p_m and compare it to the likelihood gained over a baseline model. This baseline assumes cells to be independent and characterized by their firing rate $p_r(\mathbf{x}) = \prod_i (r_i x_i + (1 - r_i)(1 - x_i))$ with rates r_i for individual cells i . The independent model is easily estimated and normalized, and is commonly used as a reference for model comparison. The excess log likelihood over this baseline is defined in terms of an expectation per unit time as $\mathcal{L} = \frac{1}{N\tau} \sum_{\mathbf{x} \in \mathcal{D}} [\log_2 p_m(\mathbf{x}) - \log_2 p_r(\mathbf{x})]$, where τ is the width of a time bin. The excess log likelihood rate \mathcal{L} , measured in bits/s, is used as the basis for model comparisons.

3 Results

We estimated Ising, RBM and sRBM models for populations of cortical cells simultaneously recorded across all cortical layers in a microcolumn. Here we present data from two animals, one with 23 single units (B4), another with 36 units (T6), as well as a multiunit recording with 28 units (B4MU). In each case the population was verified to be visually responsive and the majority of cells were orientation selective simple or complex cells.

The estimated model parameters for the three different types of models (Ising, RBM and sRBM) are shown in Fig. 2. The sparseness penalty, chosen to optimize likelihood on a validation dataset, results in many of the parameters being zero. For the Ising model (a) we show the coupling as a matrix plot, with horizontal lines indicating anatomical layer boundaries. The diagonal contains the bias terms (there is no self-coupling), which are negative since all cells are off the majority of the time. The matrix has many small positive weights that encourage positive pairwise correlations by lowering the energy of connected states being active simultaneously.

In (b) we show the hidden units of the RBM as individual bar plots, with the bars representing connection strengths to visible units. The topmost bar corresponds to the hidden bias of the unit. Hidden units are ordered by variance. The units are highly selective in connectivity: The first unit almost exclusively connects to cells in the deep (granular and subgranular) cortical layers. The second and third unit capture correlations between cells in the superficial (supergranular) layers. The correlations are of high order, with 10 and more cells receiving input from a hidden unit. The remaining units connect fewer cells, but still tend to be location-specific. Unit five captures a predominantly pairwise correlation that is also visible in the Ising model coupling matrix. Only six out of the total 23 hidden units have non-zero couplings and are shown. Additional hidden units are disabled by the L1 sparseness penalty, which was chosen to maximize likelihood on the cross-validation dataset. The interpretation of hidden units is quite similar to the pairwise terms of the Ising model: positive coupling to a group of visible units encourages these units to become active simultaneously, as the energy of the system is lowered if both the hidden unit and the cells it connects to are active. Thus the hidden units become switched on when cells they connect to are firing (activation of hidden units not shown).

The sRBM combines both pairwise and hidden connections and hence is show with a pairwise coupling matrix and bar plots for hidden units. Due to the larger number of parameters, the optimal model is even more sparse. The remaining pairwise terms now predominantly encode negative interactions, whereas much of the positive coupling has been explained away by the hidden units. These still provide strong positive couplings within either superficial (II/III) or intermediate (IV) and deep (V/VI) layers, which explain the majority of structure in the data.

It is noteworthy that the preferred explanation for dependencies between recorded neurons is via connections to shared hidden units, rather than direct couplings between visible units. The RBM

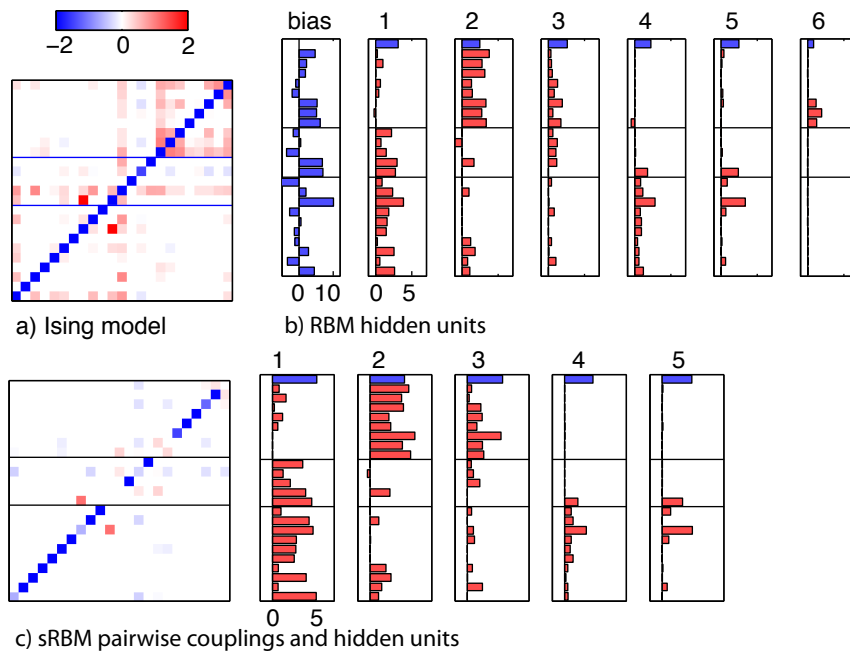


Figure 2: Connectivity patterns of the three models estimated for a recording session with 23 spike sorted single units. The horizontal lines indicate approximate boundaries between cortical layers II/III, layer IV and layers V/VI. **(a)** Ising model with the bias terms on the diagonal. The model has many small coupling terms that encode positive correlations. **(b)** The RBM coupling weights are plotted as a bar chart for each hidden unit, ordered by activity from left to right. The first bar chart is the bias for all the visible units, and the extra bar at the top of each plot corresponds to the bias of that hidden unit. Blue bars indicate a sign flip (the bias terms are predominantly negative, but plotted with reversed sign for easier comparison with the remaining terms). **(c)** The sRBM weights are shown in the same way, with the pairwise couplings on the left and hidden units on the right. The pairwise connections are qualitatively very different from those of the Ising model, as most of the structure is better captured by hidden units.

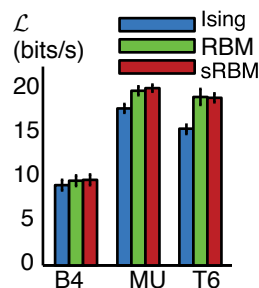


Figure 3: **(a)** Model comparison using likelihood gain over the independent (firing rate) model. Likelihoods are normalized to bits/s, but not for model size, explaining the large difference between data sets of different size: 23 cells for session B4, 28 cells for MU, and 36 cells for T6. B4 and T6 are spike sorted, MU is a multiunit dataset. All three models outperform the independent model by 10-20 bits/s. The higher order models with hidden units give a further improvement of about 2 bit/s over the Ising model.

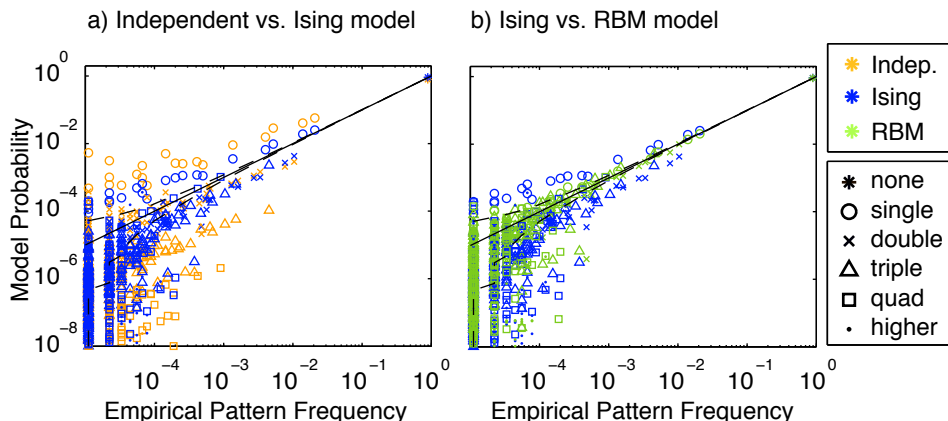


Figure 4: Scatter plot of test data set showing empirical probabilities against model probabilities. Different models are encoded by color, the number of simultaneously spiking cells in each pattern by different symbols. **(a)** shows the independent model compared to the Ising model, **(b)** shows the Ising model compared to the RBM. The sRBM is omitted as it is very similar to the RBM. The RBM significantly outperforms simpler models.

and sRBM in this comparison were both estimated with 25 hidden units, but we show only units that did not go to zero due to the sparseness constraint. In this case, $\lambda = 2 \times 10^{-3}$ was found to be optimal. Since at this level of sparseness, many of the hidden units turn off entirely, it was deemed unnecessary to further increase the number of hidden units.

For a quantitative comparison between models, we computed normalized likelihoods using AIS to estimate the partition function. For each model, we generated 500 samples through a chain of 10^5 annealing steps. To ensure convergence of the chain, we use a series of chains varying the number of annealing steps and verify that the estimate of Z stabilizes to within at least 0.02 bits/bin (see supplemental Fig. 7 in the Appendix). For models of size 20 and smaller we furthermore computed the partition function exactly to compare against the AIS estimate.

Fig. 3 a) shows a comparison of excess log likelihood \mathcal{L} over the independent firing rate model for the three different models and on all three datasets. \mathcal{L} is computed in units of bits/s for the full population. Both higher-order models outperform the Ising model in fitting the datasets, significantly so for two datasets. Error bars are standard error on the mean, computed from 10 models with different random subsets of the data used for learning and validation, and different random seeds for the parameters and the AIS sampling runs. Each of the models was estimated for a range of sparseness parameters $\lambda = [0, 1, 2, 4, 6, 8, 10] \times 10^{-3}$ bracketing the optimal λ , and the results are shown for the optimal choice of λ for each model.

Additional insight into the relative performance of the models can be gained by comparing model probabilities to empirical probabilities for the various types of patterns. Fig. 4 shows scatter plots of model probabilities under the different models against pattern frequencies in the data. Patterns with a single active cell, two simultaneously active cells, etc. are distinguished by different symbols. As expected from the positive correlations, the independent model (yellow) shown in a) has to greatly overestimate the probabilities of cells being active individually, so these patterns fall above the identity line, while all other patterns are underestimated. For comparison the Ising model is shown in the same plot (blue), and does significantly better, indicated by the points moving closer to the identity line. It still tends to fail in a similar way though, with many of the triplet patterns being underestimated as the model cannot capture triplet correlations. In b), this model is directly compared against the RBM (green). Except for very rare patterns, most points are now very close to the identity line, as the model can fully capture higher order dependencies. Hidden units describe global dependencies that greatly increase the frequency of high order patterns compared to individually active cells. The 5% and 95% confidence intervals for the counting noise expected in the empirical frequency of system states are shown as dashed lines. The solid line is the identity.

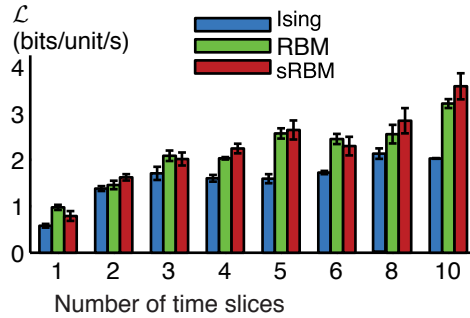


Figure 5: Likelihood comparison as a function of model size, for spatiotemporal models with 10 cells and a varying number of concatenated time steps. The log-likelihood per neuron increases as each neuron is modeled as part of a longer time sequence. This effect holds both for Ising and higher order models, but since the Ising model cannot capture many of the relevant dependencies, the increase in likelihood saturates at about 3 timesteps.

Note that any error in estimating the partition function of the models would lead to a vertical offset of all points. Thus visually checking the alignment of the data cloud around the identity line provides an intuitive verification that there are no catastrophic errors in the estimation of the partition function. Unfortunately we cannot use this alignment (e.g. of the most frequent all zeros state) as a shortcut to compute the partition function without sampling: L_1 regularization tends to reduce model probabilities of the most frequent states, so this estimate of Z would systematically overestimate the likelihood of regularized models. We note, however, that for models with no regularization this estimate does indeed agree well with the AIS estimate.

3.1 Spatiotemporal models

The same models can be used to capture spatiotemporal patterns by treating previous time steps as additional cells. Consecutive network states binned at 6.7ms are concatenated in blocks of up to 10 time steps, for a total network dimensionality of 100 with 10 cells. These models were cross-validated and the sparseness parameters optimized in the same way as for the instantaneous model. This allows us to learn kernels that describe the temporal structure of interactions between cells.

In Fig. 5 we compare the relative performance of spatiotemporal Ising and higher order models as a function of the number of time steps included in the model. To create the datasets, we picked a subset of 10 cells with the highest firing rates from the B4 dataset (4 cells from subgranular, 2 from granular and 4 from supergranular layers) and concatenated blocks of up to 10 subsequent data vectors. This way models of any dimensionality divisible by 10 can be estimated. The number of parameters of the RBM and Ising model were kept the same by fixing the number of hidden units in the RBM to be equal to the number of visible units, the sRBM was also estimated with a square weight matrix for the hidden layer. As before, the higher order models consistently outperform the Ising model. The likelihood per unit increases with the network size for all models, as additional information from network interactions leads to an improvement in the predictive power of the model. However, the curve levels off for the Ising model after a dimensionality of about 30 is reached, as higher order structure that is not well captured by the Ising model becomes increasingly important.

A similar observation has been made in [4], where Ising and higher order models for 100 retinal ganglion cells were compared to models for 10 time steps of 10 cells. It is noteworthy that temporal dependencies are similar to dependencies between different cells, in that there are strong higher order correlations not well described by pairwise couplings. These dependencies extend surprisingly far across time (at least 67ms, corresponding to the largest models estimated here) and are of such a form that including pairwise couplings to these states does not increase the likelihood of the model. This has implications e.g. for GLMs that are typically estimated with linear spike coupling kernels which will miss these interactions.

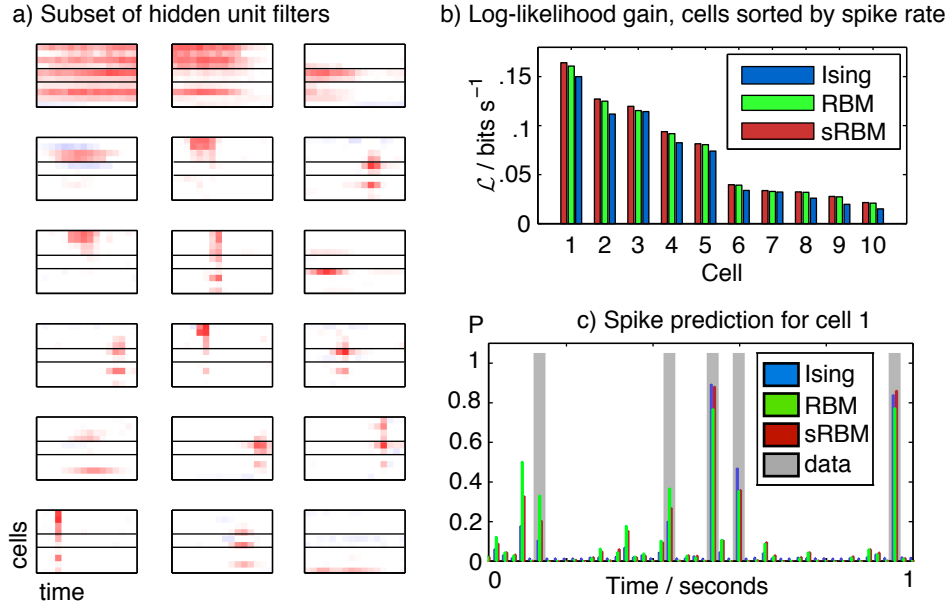


Figure 6: **(a)** Hidden units of spatiotemporal sRBM model. For each hidden unit, the horizontal axis is time and the vertical axis cells with horizontal bars separating the subgranular, granular and supergranular cortical layers. **(b)** Log-likelihood gain for one cell conditioned on the network state for all three models. The remaining population carries more information about cells with higher firing rates. **(c)** Spike prediction from network history. For one of the cells, we show 1s of predicted activity given the history of the network state. In each case when a spike occurs in the data, there is an elevated probability under the models.

To predict spiking based on the network history, we can compute the conditional distribution of single units given the state of the rest of the network. This is illustrated for a network with 15 time steps for a dimensionality of 150. Fig. 6 a) shows the learned weights of 18 randomly chosen hidden units for a spatiotemporal RBM model with 150 hidden units. Each subplot corresponds to one hidden unit, which connects to 10 neurons (vertical axis) across 15 time steps or 100ms (horizontal axis). Some units specialize in spatial coupling across different cells at a constant time lag. The remaining units describe smooth, long-range temporal dependencies, typically for small groups of cells. Both of these subpopulations capture higher order structure connecting many neurons that cannot be approximated with pairwise couplings.

By conditioning the probability of one cell at one time bin on the state of the remaining network, we can compute how much information about a cell is captured by the model over a naive prediction based on the firing rate of the cell. This conditional likelihood for each cell is plotted in 6 b) in a similar way to excess log likelihood for the entire population in Fig. 5. While the result here reflects our previous observation that Boltzmann machines with hidden units outperform Ising models, we note that the conditional probabilities are easily normalized in closed form since they describe a one-dimensional state space. Thus we can ensure that the likelihood gain holds independent of the estimation of Z and cannot be due to systematic errors in sampling from the high-dimensional models. Fig. 6 c) provides a more intuitive look at the prediction. For 1s of data from one cell, where 5 spikes occur, we show the conditional firing probabilities for the 3 models given 100ms of history of itself and the other cells. Qualitatively, the models perform well in predicting spiking probabilities, suggesting it might compare favorably to prediction based on GLM-type or Ising models [24].

4 Discussion

We explored the utility of Boltzmann machines with hidden units as models for neural population data, arguing that it provides a better model for cortical data than Ising models and previous extensions. While there has been a resurgence of interest in these maximum entropy models for describing neural data, progress has been hampered mainly by two problems: Estimation of energy based models is difficult since these models cannot be normalized in closed form. Evaluating the likelihood of the model thus requires approximations or a numerical integral over the exponential number of states of the model, making maximum likelihood estimation computationally intractable. Therefore even the pairwise Ising model is hard to estimate in general, and various approximations have been used to overcome this problem. This is a purely computational difficulty, but there is a more fundamental issue with generalizing models to include higher order dependencies. While this does not by itself make the model estimation any more difficult, in general the number of model parameters to be estimated is now also exponential in the size of the data. This can be dealt with either by cutting off dependencies at some low order, estimating only a small number of higher order coupling terms, or by imposing some specific form on the dependencies.

We attempted to address both of these problems here. Parameter estimation was made tractable using MPF, and latent variables were shown to be an effective way of capturing high order dependencies. This addresses several shortcomings that have been identified with the Ising model.

As Macke argues in [25], models with direct (pairwise) couplings are not well suited to model data recorded from cortical networks. Since only a tiny fraction of the neurons making up the circuit are recorded, most input is likely to be common input to many of the recorded cells rather than direct synapses between them. While his work compares Generalized Linear Models (GLMs) such as models of the retina [26] and for LGN [27] to linear dynamical systems (LDS) models, the argument applies equally for the models presented here.

Another shortcoming of the Ising model and some previous extensions is that the number of parameters to be estimated does not scale favorably with the dimensionality of the network. The number of pairwise coupling terms in GLM and Ising models scales with the square of the number of neurons, so with the amounts of data typically collected in electrophysiological experiments it is only possible to identify the parameters for small networks with a few tens of cells. This problem is aggravated by including higher order couplings: for example the number of third order coupling parameters scales with the cube of the data dimensionality. Therefore attempting to estimate these coupling parameters directly is a daunting task that usually requires approximations and strong regularization.

An alternative is to focus on higher order structure in very small networks. Ohiorhenuan noted that Ising models fail to explain structure in cat visual cortex [7] and was able to model triplet correlations [8] by considering very small populations of no more than 6 neurons. However, Schneidman and Gammor caution [4] that trying to model small subsets (10 cells) of a larger network to infer properties of the full network may lead to wrong conclusions and show that for retinal networks higher order correlations start to dominate only once a certain network size is reached. Therefore they address the same question as the present paper, i.e. how to capture n^{th} order correlations without the accompanying d^n growth in the number of free parameters in a larger network. In their proposed *reliable interaction model*, they exploit the sparseness of the neural firing patterns to argue that most higher order coupling terms will be zero. Therefore the true distribution can be well approximated from a small number of these terms, which can be calculated using a simple recursive scheme. In practice, the main caveat is that only patterns that appear in the data many times are used to calculate the coupling terms. While the model by construction assigns correct relative probabilities to observed patterns, the probability assigned to unobserved patterns is unconstrained, and the most probable states may therefore be ones which never occur in the data.

In contrast to these models focussed on retinal data however, in visual cortex higher order correlations play an important role even in small networks. Yu et al. [3, 9] show that over the scale of adjacent cortical columns of anesthetized cat visual cortex, small subnetworks of 10 cells are better characterized with a dichotomized Gaussian model than the pairwise maximum entropy distribution. While the dichotomized Gaussian [28] is estimated only from pairwise statistics, it carries higher order correlations that can be interpreted as common Gaussian inputs [29]. However these correlations are implicit in the structure of the model and not directly estimated from the data as with the RBM, so it is not clear that the model would perform as well on different datasets.

Finally, GLMs [26] can be used to model each cell conditioned on the rest of the population. While mostly used for stimulus response models including stimulus terms, they are easily extended with terms for cross-spike coupling, which capture interactions between cells. A major limitation of GLMs is that current implementations can only be estimated efficiently if they are linear in the stimulus features and network coupling terms, so they are not easily generalized to higher order interactions. Two approaches have been used to overcome this limitation for stimulus terms. The GLM can be extended with additional nonlinearities, preserving convexity on subproblems [27]. Alternatively, the stimulus terms can be packaged into nonlinear features which are computed in preprocessing and usually come with the penalty of a large increase in the dimensionality of the problem [30]. However, we are not aware of any work applying either of these ideas to spike history rather than stimulus terms. Another noteworthy drawback of GLMs is that instantaneous coupling terms cannot be included as this causes probabilities to diverge [25], so instantaneous correlations cannot be modeled and have to be approximated using very fine temporal discretization.

In conclusion, the RBM provides a parsimonious model for higher order dependencies in neural population data. Without explicitly enumerating a potentially exponential number of coupling terms or being constrained by only measurements of pairwise correlations, it provides a low-dimensional, physiologically interpretable model that can be easily estimated for populations of 100 and more cells.

The connectivity patterns the RBM learns from cells simultaneously recorded from all cortical layers are spatially localized, showing that small neural assemblies within cortical layers are strongly coupled. This suggests a shared computation these local networks perform on common input, while cells across different cortical layers participate in distinct computations and have much less coupled activity. This novel observation is made possible by the RBM: because each of the hidden units responds to (and therefore learns on) a large number of recorded patterns, it can capture dependencies that are too weak to extract with previous models. In particular, the connectivity patterns discovered by the RBM and sRBM are by no means obvious from the covariance of the data or by inspecting the coupling matrix of the Ising model. This approach, combining a straightforward estimation procedure and a powerful model, can be extended from polytrode recordings to capture physiologically meaningful connectivity patterns in other types of multi-electrode data.

Acknowledgments

BAO, CMG and UK were supported by National Eye Institute grant #EY019965.

References

- [1] Ernst Ising. Beitrag zur Theorie des Ferromagnetismus. *Zeitschrift für Physik A*, 31(1):253–258, 1925.
- [2] Elad Schneidman, Michael J Berry, Ronen Segev, and William Bialek. Weak pairwise correlations imply strongly correlated network states in a neural population. *Nature*, 440(7087):1007–12, April 2006.
- [3] Shan Yu, Debin Huang, Wolf Singer, and Danko Nikolic. A Small World of Neuronal Synchrony. *Cerebral Cortex*, 18(12):2891–2901, 2008.
- [4] Elad Ganmor, Ronen Segev, and Elad Schneidman. Sparse low-order interaction network underlies a highly correlated and learnable neural population code. *Proceedings of the National Academy of Sciences of the United States of America*, 108(23):9679–84, June 2011.
- [5] Alexander S Ecker, Philipp Berens, Georgios Keliris, Matthias Bethge, Nikos K Logothetis, and Andreas S Tolias. Decorrelated neuronal firing in cortical microcircuits. *Science (New York, N.Y.)*, 327(5965):584–7, January 2010.
- [6] Alfonso Renart, J. De la Rocha, Peter Bartho, Liad Hollender, N. Parga, Alex Reyes, and K.D. Harris. The asynchronous state in cortical circuits. *Science*, 327(5965):587–590, 2010.
- [7] Ifije E Ohiorhenuan, Ferenc Mechler, Keith P Purpura, Anita M Schmid, Qin Hu, and Jonathan D Victor. Sparse coding and high-order correlations in fine-scale cortical networks. *Nature*, 466(7306):617–21, July 2010.

- [8] Ifije E Ohiorhenuan and Jonathan D Victor. Information-geometric measure of 3-neuron firing patterns characterizes scale-dependence in cortical networks. *Journal of computational neuroscience*, 30(1):125–41, March 2011.
- [9] Shan Yu, Hongdian Yang, Hiroyuki Nakahara, Gustavo Santos, Danko Nicolic, and Dietmar Plenz. Higher-order interactions characterized in cortical activity. *The Journal of Neuroscience*, 31(48):17514–17526, 2011.
- [10] K J Stratford, K Tarczy-Hornoch, K A Martin, N J Bannister, and J J Jack. Excitatory synaptic inputs to spiny stellate cells in cat visual cortex. *Nature*, 382(6588):258–261, July 1996.
- [11] GM Ghose, RD Freeman, and I Ohzawa. Local intracortical connections in the cat’s visual cortex: postnatal development and plasticity. *Journal of Neurophysiology*, 72(3):1290–303, 1994.
- [12] Jascha Sohl-Dickstein, Peter Battaglino, and Michael DeWeese. Minimum Probability Flow Learning. In *International Conference on Machine Learning*, 2011.
- [13] Jascha Sohl-Dickstein, Peter Battaglino, and Michael DeWeese. New Method for Parameter Estimation in Probabilistic Models: Minimum Probability Flow. *Physical Review Letters*, 107(22):11–14, November 2011.
- [14] MT Schaub. The Ising decoder: reading out the activity of large neural ensembles. *Journal of computational neuroscience*, 2012.
- [15] RM Neal. Annealed importance sampling. Technical report, University of Toronto, Toronto, 2001.
- [16] KD Harris, DA Henze, Jozsef Csicsvari, Hajime Hirase, and Gyorgy Buzsaki. Accuracy of Tetrode Spike Separation as Determined by Simultaneous Intracellular and Extracellular Measurements. *Journal of Neurophysiology*, 84(1):401–414, 2000.
- [17] David Redish. MClust. Technical report, University of Minnesota, Minneapolis, 2012.
- [18] U Mitzdorf. Current source-density method and application in cat cerebral cortex: investigation of evoked potentials and EEG phenomena. *Physiological reviews*, 65(1):37–100, January 1985.
- [19] Charles M Gray, Pedro E Maldonado, M Wilson, and Bruce McNaughton. Tetrodes markedly improve the reliability and yield of multiple single-unit isolation from multi-unit recordings in cat striate cortex. *Journal of neuroscience methods*, 63(1-2):43–54, December 1995.
- [20] Simon Osindero and Geoffrey Hinton. Modeling image patches with a directed hierarchy of Markov random fields. *Advances in neural information processing*, pages 1–8, 2008.
- [21] Geoffrey E Hinton. Training products of experts by minimizing contrastive divergence. *Neural computation*, 14(8):1771–800, August 2002.
- [22] Mark Schmidt. MinFunc. Technical report, Laboratoire d’Informatique de l’École Normale Supérieure, Paris, 2005.
- [23] Ruslan Salakhutdinov and Iain Murray. On the quantitative analysis of deep belief networks. In *ICML*, 2008.
- [24] Wilson Truccolo, Leigh R Hochberg, and John P Donoghue. Collective dynamics in human and monkey sensorimotor cortex : predicting single neuron spikes. *Nature Neuroscience*, 13(1):105–111, 2009.
- [25] Jakob H Macke, John P Cunningham, Krishna V Shenoy, and Maneesh Sahani. Empirical models of spiking in neural populations. In *Advances in Neural Information Processing*, pages 1–9, 2011.
- [26] Jonathan W Pillow, Jonathon Shlens, Liam Paninski, Alexander Sher, Alan M Litke, E J Chichilnisky, and Eero P Simoncelli. Spatio-temporal correlations and visual signalling in a complete neuronal population. *Nature*, 454(7207):995–9, August 2008.
- [27] D. Butts, C. Weng, J. Jin, J.-M. Alonso, and L. Paninski. Temporal Precision in the Visual Pathway through the Interplay of Excitation and Stimulus-Driven Suppression. *Journal of Neuroscience*, 31(31):11313–11327, August 2011.
- [28] Jakob H Macke, Philipp Berens, Alexander S Ecker, Andreas S Tolias, and Matthias Bethge. Generating spike trains with specified correlation coefficients. *Neural computation*, 21(2):397–423, February 2009.

- [29] J Macke, Iain Murray, and PE Latham. How biased are maximum entropy models? *Advances in neural information processing*, pages 1–11, 2011.
- [30] Sebastian Gerwinn, Jakob H Macke, and Matthias Bethge. Bayesian inference for generalized linear models for spiking neurons. *Frontiers in computational neuroscience*, 4(May):12, January 2010.
- [31] Aapo Hyvärinen. Estimation of non-normalized statistical models by score matching. *Journal of Machine Learning Research*, 6:695–709, 2006.
- [32] Aapo Hyvärinen. Some extensions of score matching. *Computational statistics & data analysis*, 51(5), 2007.
- [33] Michael Gutmann. Noise-contrastive estimation : A new estimation principle for unnormalized statistical models. *Journal of Machine Learning Research*, pages 297–304, 2009.

A Marginalizing over hidden units

In this section we review how the joint probability for visible and hidden units in the RBM can be integrated in closed form to obtain the marginal distribution for the visible units. First we rewrite the sum over hidden variables as a product

$$p(\mathbf{x}, \mathbf{h}) = \frac{1}{Z} \exp \left(\sum_{i,j} x_i h_j w_{ij} + \sum_i x_i a_i + \sum_j h_j b_j \right) \quad (10)$$

$$= \frac{1}{Z} e^{\sum_i x_i a_i} \prod_{j=1}^M \exp \left(\sum_i x_i h_j w_{ij} + h_j b_j \right) \quad (11)$$

and integrate $p(\mathbf{x}) = \sum_{\{h\}} p(\mathbf{x}, \mathbf{h})$, where the sum is over all configurations of the hidden units. For the purpose of this derivation, we move the first term outside the product

$$p(\mathbf{x}) = \frac{1}{Z} e^{\sum_i x_i a_i} \sum_{\{h\}} \exp \left(\sum_i x_i h_1 w_{i1} + h_1 b_1 \right) \prod_{j=2}^M \exp \left(\sum_i x_i h_j w_{ij} + h_j b_j \right). \quad (12)$$

We can write the sum over all hidden states as nested sums over every state for each hidden unit

$$p(\mathbf{x}) = \frac{1}{Z} e^{\sum_i x_i a_i} \sum_{h_1 \in \{0,1\}} \dots \sum_{h_m \in \{0,1\}} \exp \left(\sum_i x_i h_1 w_{i1} + h_1 b_1 \right) \quad (13)$$

$$\prod_{j=2}^M \exp \left(\sum_i x_i h_j w_{ij} + h_j b_j \right). \quad (14)$$

Noting that the term we have singled out appears only in one of the sums, we rearrange to isolate the sum,

$$p(\mathbf{x}) = \frac{1}{Z} e^{\sum_i x_i a_i} \sum_{h_1 \in \{0,1\}} \exp \left(\sum_i x_i h_1 w_{i1} + h_1 b_1 \right) \quad (15)$$

$$\sum_{h_2 \in \{0,1\}} \dots \sum_{h_m \in \{0,1\}} \prod_{j=2}^M \exp \left(\sum_i x_i h_j w_{ij} + h_j b_j \right). \quad (16)$$

Doing this for all terms we obtain a product over individual one-dimensional sums

$$p(\mathbf{x}) = \frac{1}{Z} e^{\sum_i x_i a_i} \prod_{j=1}^M \sum_{h_j \in \{0,1\}} \exp \left(\sum_i x_i h_j w_{ij} + h_j b_j \right) \quad (17)$$

$$= \frac{1}{Z} e^{\sum_i x_i a_i} \prod_{j=1}^M \left[1 + \exp \left(\sum_i x_i w_{ij} + b_j \right) \right] \quad (18)$$

$$= \frac{1}{Z} \exp \left(\sum_i x_i a_i \sum_{j=1}^M \log \left[1 + \exp \left(\sum_i x_i w_{ij} + b_j \right) \right] \right). \quad (19)$$

The marginal distribution over \mathbf{x} for the RBM is now in the form of a standard energy based model, with energy function

$$E(\mathbf{x}) = - \sum_i x_i a_i - \sum_{j=1}^M \log \left[1 + \exp \left(\sum_i x_i w_{ij} + b_j \right) \right]. \quad (20)$$

The sRBM follows the same logic, since additional terms in the energy that do not depend on the hidden units stay outside the sum over hidden configurations in the same fashion as for the visible bias.

B MPF objective

B.1 Ising model

Here we review the derivation of the MPF objective for an Ising model, where the objective function consists of terms connecting the data states to all states which differ by a single bit flip.

The general MPF objective function is given by

$$K(\Theta) = \sum_{\mathbf{x} \in \mathcal{D}} \sum_{\mathbf{x}' \notin \mathcal{D}} g(\mathbf{x}, \mathbf{x}') \exp \left(\frac{1}{2} [E(\mathbf{x}; \Theta) - E(\mathbf{x}'; \Theta)] \right), \quad (21)$$

where $g(\mathbf{x}, \mathbf{x}') = g(\mathbf{x}', \mathbf{x}) \in \{0, 1\}$ is the connectivity function, $E(\mathbf{x}; \Theta)$ is an energy function parameterized by Θ , and \mathcal{D} is the list of data states. We consider the case where the connectivity function $g(\mathbf{x}, \mathbf{x}')$ is set to connect all states which differ by a single bit flip,

$$g(\mathbf{x}, \mathbf{x}') = \begin{cases} 1 & \mathbf{x} \text{ and } \mathbf{x}' \text{ differ by a single bit flip, } \sum_n |x_n - x'_n| = 1 \\ 0 & \text{otherwise} \end{cases} \quad (22)$$

The MPF objective function in this case is

$$K(\Theta) = \sum_{\mathbf{x} \in \mathcal{D}} \sum_{n=1}^N \exp \left(\frac{1}{2} [E(\mathbf{x}; \Theta) - E(\mathbf{x} + \mathbf{d}(\mathbf{x}, n); \Theta)] \right) \quad (23)$$

where the sum over n is a sum over all data dimensions, and the bit flipping function $\mathbf{d}(\mathbf{x}, n) \in \{-1, 0, 1\}^N$ is

$$\mathbf{d}(\mathbf{x}, n)_i = \begin{cases} 0 & i \neq n \\ -(2x_i - 1) & i = n \end{cases} \quad (24)$$

For the Ising model, the energy function is

$$E = \mathbf{x}^T \mathbf{J} \mathbf{x} \quad (25)$$

where $\mathbf{x} \in \{0, 1\}^N$, $\mathbf{J} \in \mathcal{R}^{N \times N}$, and \mathbf{J} is symmetric ($\mathbf{J} = \mathbf{J}^T$). The bias terms have been absorbed into the diagonal of the matrix \mathbf{J} which is possible since $x^2 = x$ holds for binary x .

Substituting this energy into the MPF objective function, it becomes

$$K = \sum_{\mathbf{x} \in \mathcal{D}} \sum_n \exp \left(\frac{1}{2} [\mathbf{x}^T \mathbf{J} \mathbf{x} - (\mathbf{x} + \mathbf{d}(\mathbf{x}, n))^T \mathbf{J} (\mathbf{x} + \mathbf{d}(\mathbf{x}, n))] \right) \quad (26)$$

$$= \sum_{\mathbf{x} \in \mathcal{D}} \sum_n \exp \left(\frac{1}{2} [\mathbf{x}^T \mathbf{J} \mathbf{x} - (\mathbf{x}^T \mathbf{J} \mathbf{x} + 2\mathbf{x}^T \mathbf{J} \mathbf{d}(\mathbf{x}, n) + \mathbf{d}(\mathbf{x}, n)^T \mathbf{J} \mathbf{d}(\mathbf{x}, n))] \right) \quad (27)$$

$$= \sum_{\mathbf{x} \in \mathcal{D}} \sum_n \exp \left(-\frac{1}{2} [2\mathbf{x}^T \mathbf{J} \mathbf{d}(\mathbf{x}, n) + \mathbf{d}(\mathbf{x}, n)^T \mathbf{J} \mathbf{d}(\mathbf{x}, n)] \right) \quad (28)$$

$$= \sum_{\mathbf{x} \in \mathcal{D}} \sum_n \exp \left(-\frac{1}{2} \left[2 \sum_i x_i J_{in} (1 - 2x_n) + J_{nn} \right] \right) \quad (29)$$

$$= \sum_{\mathbf{x} \in \mathcal{D}} \sum_n \exp \left(\left[(2x_n - 1) \sum_i x_i J_{in} - \frac{1}{2} J_{nn} \right] \right). \quad (30)$$

Assume the symmetry constraint on \mathbf{J} is enforced by writing it in terms of a another possibly asymmetric matrix $\mathbf{J}' \in \mathcal{R}^{N \times N}$,

$$\mathbf{J} = \frac{1}{2}\mathbf{J}' + \frac{1}{2}\mathbf{J}'^T. \quad (31)$$

The derivative of the MPF objective function with respect to \mathbf{J}' is

$$\begin{aligned} \frac{\partial K}{\partial J'_{lm}} = & \frac{1}{2} \sum_{\mathbf{x} \in \mathcal{D}} \exp \left(\left[(2x_m - 1) \sum_i x_i J_{im} - \frac{1}{2} J_{mm} \right] \left[(2x_m - 1) x_l - \delta_{lm} \frac{1}{2} \right] \right. \\ & \left. + \frac{1}{2} \sum_{\mathbf{x} \in \mathcal{D}} \exp \left(\left[(2x_l - 1) \sum_i x_i J_{il} - \frac{1}{2} J_{ll} \right] \left[(2x_l - 1) x_m - \delta_{ml} \frac{1}{2} \right] \right), \end{aligned} \quad (32)$$

where the second term is simply the first term with indices l and m reversed.

B.2 RBM

After marginalizing out the hidden units, the energy function over the visible units for an RBM is given by:

$$E(\mathbf{x}) = - \sum_i \log(1 + e^{-W_i \mathbf{x}}) \quad (33)$$

where W_i is a vector of coupling parameters and \mathbf{x} is the binary input vector. Bias terms have been omitted for readability.

As previously, we substitute into the objective function Eq. 23 to obtain

$$K = \sum_{\mathbf{x} \in \mathcal{D}} \sum_n \exp \left(\frac{1}{2} \left[- \sum_i \log(1 + e^{-W_i \mathbf{x}}) + \sum_i \log(1 + e^{-W_i \mathbf{x} + W_i \mathbf{d}(\mathbf{x}, n)}) \right] \right). \quad (34)$$

Unlike for the Ising model there is no cancellation of data and non-data energy terms, so evaluating the function and derivative requires looping over all bit flips for the data set.

B.3 sRBM

The energy function over the visible units for an sRBM obtained by marginalizing out the conditionally independent hidden units is

$$E(\mathbf{x}; \mathbf{J}, \mathbf{W}) = \mathbf{x}^T \mathbf{J} \mathbf{x} - \sum_i \log(1 + e^{-\mathbf{w}_i^T \mathbf{x}}) \quad (35)$$

where $\mathbf{x} \in \{0, 1\}^N$ is the visible state, $\mathbf{J} = \mathbf{J}^T \in \mathcal{R}^{N \times N}$ is a symmetric coupling matrix, and $\mathbf{W} \in \mathcal{R}^{M \times N}$ is a weight matrix to M hidden units. Equation 35 consists of a term capturing connections between visible units (an Ising model), and a term capturing connections to hidden units (an RBM).

The MPF objective we use again consists of energy differences between data and non-data states differing by a single bit. For the RBM this energy difference with the n^{th} bit flipped is

$$dE_n^R = - \sum_i \left[\log(1 + e^{-\mathbf{w}_i^T \mathbf{x}}) - \log(1 + e^{-\mathbf{w}_i^T (\mathbf{x} + \mathbf{d}(\mathbf{x}, n))}) \right] \quad (36)$$

$$= - \sum_i \left[\log(1 + e^{z_i}) - \log(e^{z_i} + e^{w_{in} b_n}) \right] \quad (37)$$

where for notational simplicity we have defined $z_i = \mathbf{w}_i^T \mathbf{x}$ and $b = 2\mathbf{x} - 1$. The energy difference contributed by connections between visible units (the Ising model) is

$$dE_n^I = 2b_n y_n - \frac{1}{2} J_{nn} \quad (38)$$

where we define the shorthand $\mathbf{y} = \mathbf{J}\mathbf{x}$ for simplicity. The total objective function is then given by a sum over samples and bit flips as

$$K = \sum_{\mathbf{x} \in \mathcal{D}} \sum_n \exp \left[\frac{1}{2} (dE_n^I + dE_n^R) \right] \quad (39)$$

To compute the gradient of this objective w.r.t. the parameters W and J we note that

$$\frac{\partial K}{\partial J} = \sum_{\mathbf{x} \in \mathcal{D}} \sum_n K_n \frac{\partial}{\partial J} dE_n^I \quad (40)$$

$$\frac{\partial K}{\partial W} = \sum_{\mathbf{x} \in \mathcal{D}} \sum_n K_n \frac{\partial}{\partial W} dE_n^R \quad (41)$$

these terms are computed as

$$\frac{\partial}{\partial J} dE_n^I = \frac{\partial}{\partial J} \left(2b_n y_n - \frac{1}{2} J_{nn} \right) = 2b_n x_n - \frac{1}{2} \quad (42)$$

for the pairwise terms, and

$$\frac{\partial}{\partial W_{ab}} dE_n^R = - \frac{\partial}{\partial W_{ab}} \sum_i [\log(1 + e^{z_i}) - \log(e^{z_i} + e^{w_{in} b_n})] \quad (43)$$

$$= \frac{1}{2} \sum_n \frac{e^{z_a}}{1 + e^{z_a}} x_b \quad (44)$$

$$+ \frac{1}{2} \sum_n \frac{e^{z_a}}{e^{z_a} + e^{w_{an} b_n}} x_b \quad (45)$$

$$+ \frac{1}{2} \sum_j \frac{1}{1 + e^{z_a - w_{ab} b_b}} b_b \quad (46)$$

for the higher order terms.

C Annealed importance sampling

Estimating the normalization constant, also referred to as partition function, of an energy based probabilistic model, remains a challenging task [23]. Many approaches to make learning the parameters of energy based models tractable, such as Contrastive Divergence, MPF, Score and Ratio Matching [31, 32] do not attempt to estimate the partition function. A notable exception is Noise Contrastive Estimation [33] which treats the partition function as a parameter to be estimated, but has only been applied for continuous-valued data. Most commonly the partition function is estimated by sampling.

Using importance sampling, the partition function can be estimated by

$$Z_p / Z_q = \left\langle \frac{\tilde{p}(\mathbf{x})}{\tilde{q}(\mathbf{x})} \right\rangle_{q(\mathbf{x})} \quad (47)$$

where Z_q is the known partition function of the proposal distribution $q(\mathbf{x})$, Z_p is the partition function of interest for $p(\mathbf{x})$ and the symbol $\tilde{\cdot}$ indicates a non-normalized distribution. The angle brackets indicate a sample expectation over samples from the distribution $p(\mathbf{x})$. However, if $q(\mathbf{x})$ is not a good match to the target distribution, it takes a very large number of samples to get a good estimate. AIS uses an annealing process to gradually transform a simple proposal distribution, such as the uniform distribution, into the target distribution, leading to an accurate estimate of Z from only a small number of samples.

To assure convergence of the estimator, we run several annealing chains, increasing the number of steps in factors of 2 up to a size of 10^5 steps. We check that the final estimate of $\log_2(Z)$ does not deviate more than 0.02 from the previous estimates. This criterium was chosen since $\log_2(Z)$ appears as an additive term to \mathcal{L} , and at a bin size $\tau = 50\text{ms}$ an error of 1 bits / second in the final estimate of the likelihood was seen as an acceptable trade-off between estimation speed and accuracy. In Fig. 7, we show this convergence plot for a small 20-dimensional model, where the normalization constant was computed exactly. For larger models, where the partition function could not be calculated analytically, we monitored that the estimate stabilized to within this tolerance.

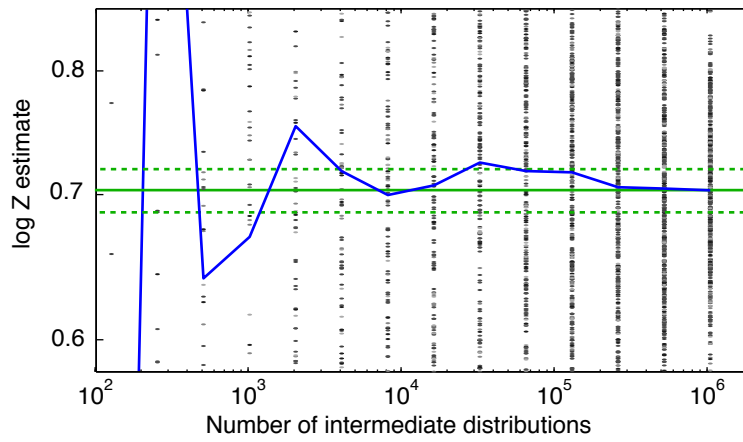


Figure 7: Monitoring the convergence of the AIS estimate for the partition function, here for a 20-dimensional Ising model. Each entry on the horizontal axis corresponds to an annealing chain with a different number of steps. Points correspond to the 500 individual samples, the blue line is the \log_2 of the average from the samples. The solid green line is the true value of the partition function computed numerically by summing over the 2^{20} states. The dashed lines correspond to our convergence criterion of 0.02 deviation from the true partition function.